Journal Pre-proofs

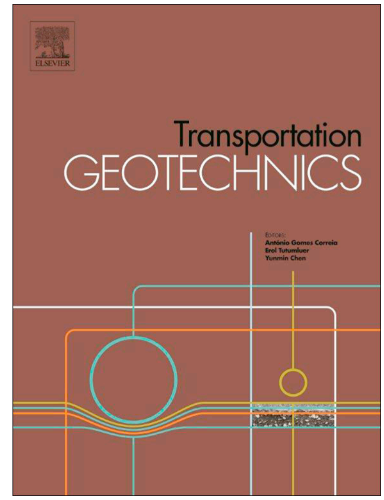

Physical and numerical investigation of integral bridge abutment stiffness due to seasonal thermal loading

Sha Luo, Ziyan Huang, Yazan Asia, Flavia De Luca, Raffaele De Risi, John Harkness, Louis Le Pen, Geoff Watson, David Milne, David Chapman, Anastasios Sextos, Nicole Metje, George Mylonakis, Nigel Cassidy, Ian Jefferson, Joel Smethurst, David Richards, Colin Taylor, William Powrie, Christopher Rogers

PII: S2214-3912(23)00137-X
DOI: https://doi.org/10.1016/j.trgeo.2023.101064
Reference: TRGEO 101064

To appear in: *Transportation Geotechnics*

Received Date: 22 April 2023
Revised Date: 24 June 2023
Accepted Date: 16 July 2023

Please cite this article as: S. Luo, Z. Huang, Y. Asia, F. De Luca, R. De Risi, J. Harkness, L. Le Pen, G. Watson, D. Milne, D. Chapman, A. Sextos, N. Metje, G. Mylonakis, N. Cassidy, I. Jefferson, J. Smethurst, D. Richards, C. Taylor, W. Powrie, C. Rogers, Physical and numerical investigation of integral bridge abutment stiffness due to seasonal thermal loading, *Transportation Geotechnics* (2023), doi: https://doi.org/10.1016/j.trgeo.2023.101064

Physical and numerical investigation of integral bridge abutment stiffness due to seasonal thermal loading

Sha Luo[1], Ziyan Huang[2], Yazan Asia[2,4], Flavia De Luca[2], Raffaele De Risi[2], John Harkness[3], Louis Le Pen[3], Geoff Watson[3], David Milne[3], David Chapman[1], Anastasios Sextos[2], Nicole Metje[1], George Mylonakis[2,5], Nigel Cassidy[1], Ian Jefferson[1], Joel Smethurst[3], David Richards[3], Colin Taylor[2], William Powrie[3], Christopher Rogers[1]

[1] School of Engineering, University of Birmingham, Edgbaston, B15 2TT (UK)

[2]School of Civil, Aerospace and Mechanical Engineering, University of Bristol, Queens Building, BS8 1TR (UK)

[3] School of Engineering, University of Southampton, Southampton, UK

[4]Department of Engineering, University of Cambridge, UK

[5] Department of Civil Infrastructure and Environmental Engineering Khalifa University, Abu Dhabi, UAE

Abstract

Integral Abutment Bridges (IABs) are increasingly popular due to their reduced maintenance cost compared to traditional bridges with expansion joints. However, the widespread construction of IABs is currently limited by design code prescriptions resulting from the significant uncertainties associated with how the backfill interacts with the (integral) abutment and the deck. Under cycles of seasonal thermal loading, the backfill properties change, affecting the distribution of lateral earth pressures acting on the abutment walls. Moreover, the stiffness of the abutment can significantly influence the soil-structure interaction (SSI) in IABs. This research work investigates the effect of abutment stiffness (flexural rigidity) on soil-structure interaction in IABs under seasonal thermal loading through experimental analyses and numerical modelling. To better understand this mechanism and reliably assess the performance of IABs within their life cycle, a 1g small-scale instrumented physical model was built to simulate the backfill under accelerated seasonal expansion and contraction of the bridge deck. The experimental results were modelled numerically in PLAXIS and ABAQUS to assess the sensitivity to different flexural stiffnesses of the abutment and discuss suitable options for modelling such SSI systems through finite elements either using a geotechnical-oriented or a structural-oriented software package. It was found that flexible IABs can be more suitable for controlling earth pressure built-up within the early lifecycle of the soil-structure systems. The simplified numerical models can provide a first-order prediction of pressure distributions in the small-scale 1-g rig. This preliminary dataset informs necessary larger-scale experiments to assess the scaling and feasibility of 1-g tests.

Keywords: Integral Bridges, thermal loading, flexural rigidity, soil-structure interaction, lateral earth pressure

1. Introduction

Integral abutment bridges (IABs) are becoming increasingly popular with significantly greater demand globally due to (i) their reduced maintenance compared to traditional bridges with expansion joints, (ii) improved seismic performance and (iii) simple and rapid construction (e.g., Burke, 2009; Alampalli and Yannotti, 1998; Civjan et al., 2007; White et al., 2010; Arsoy et al., 2004). However, the widespread construction of IABs is currently limited by the lack of internationally accepted mechanistic models and coherent design guidelines, and by code restrictions such as the maximum span length (60 m) and skew angle (30°) (BSI, 2004, 2007, 2011; HA, 2003). These limitations are mainly due to the uncertainty associated with the way the backfill interacts with the (integral) abutment and the deck in different loading scenarios during the service life, such as seasonal thermal loadings (e.g., Paul et al., 2005; Lawver et al., 2000; Sigdel, 2021; LaFave et al. 2021), daily traffic loading (e.g., Ryall et al., 2000; Petursson & Kerokoski, 2011; De Risi 2022) and seismic loading (e.g., Al-Ani et al., 2018; Dhar & Dasgupta, 2019; Fiorentino et al. 2021; Javanmardi et al. 2022). The loading from thermal actions on integral bridges is comparable in magnitude to that caused by live loads such as daily traffic loading (e.g., Neville, 1995; Lawver et al., 2000; Paul et al., 2005). Seasonal thermal loading on integral bridges here refers to the cyclic load caused by the contraction (temperature decreases during winner) and expansions (temperature increases during summer) of the deck.

In the longer term, daily and seasonal deck expansion-contraction cycles lead to a build-up of lateral earth pressures behind the abutments. According to the field monitoring data from in-service IABs, the lateral pressure behind IABs increases when sufficient displacements of the abutment are induced by thermal loading (Barker & Carder, 2000, 2001; Hassiotis et al., 2005; Breña et al., 2007; Skorpen et al., 2018). This evidence is corroborated by previous laboratory experimental research (England et al., 2000; Springman et al., 1996; Cosgrave & Lehane, 2003; Lehane, 2011). The pressure profile is influenced by several factors, such as the backfill soil stiffness and strength, compaction levels, boundary conditions, thermal loading amplitude and pile-to-abutment connection when piles are present (e.g., Dicleli and Erhan, 2004, 2005; Huffman et al., 2015; Gorini & Callisto, 2017, 2019; Xu et al., 2022; Luo et al., 2022; Liu et al. 2022). It remains unclear whether the lateral pressure behind the abutment continues building up at a specific rate before eventually stabilising and the specific influence of different flexural rigidities is also not fully covered by previous experiments.

The thermal loading also causes ground settlements adjacent to the abutments due to soil densification, strain ratcheting, and consequent horizontal sliding and the rocking motion of the abutment (Ng et al., 1998; England et al., 2000), producing gaps or cracks often observed at the surface between the abutment and backfill, which, in turn, can cause structural problems in the approaching slabs (e.g., Muttoni et al., 2013; Paraschos, 2016; Al-Ani et al., 2018; Sakhare et al. 2023). These settlements of the IAB backfill are often addressed by incorporating an approaching slab with a properly compacted backfill (Lock, 2002; Hoppe, 1999; Springman et al., 1996) or modified property materials (e.g., Dude and Siwowski 2020). In conjunction with good compaction, the backfill soil quality is also a vital factor for the SSI behaviour under multiple cycles of thermal loading (Atkinson, 2007; Carder and Hayes, 2000). The difference in the values of the backfill soil parameters (e.g., density, strength, stiffness and dilation angle) affects the development of earth pressures (Wood and Nash, 2000; Wood, 2004; England et al., 2000).

The lateral soil pressure varies with the deflection of the abutment, and, in turn, the deflection of the abutment is mainly affected by its flexural stiffness (Dicleli & Albhaisi, 2004a & 2005; Dicleli, 2005; Lehane, et al., 1999). The soil-structure interaction behaviour from the thermal expansion of IABs must be understood and analysed with a specific focus on the relative backfill/abutment stiffness (Wood and Nash, 2000; Wood, 2004). More work is needed on the specific selection of suitable stiffnesses for IABs subjected to seasonal thermal loading in different conditions. In Appendix A of PD 6694-1 (BSI, 2011), detailed guidance on soil-structure interaction analysis for an integral bridge design is provided. The effect of soil strain is accounted for by considering the soil stiffness and quasi-passive resistance, and the staged and repeated application of deck expansion and contraction is considered through an iterative procedure for the calculation of the average rotational strain. However, according to a comprehensive study carried out by Sandberg et al. (2020) pressures computed with the Limit Equilibrium (LE) approach in PD 6694-1 (BSI, 2011) were significantly higher than those computed with an SSI approach. The reduction of the stiffness of the abutment wall was suggested as a way to further reduce the predicted bending moments due to the additional flexibility of the structure (Sandberg et al., 2020). The stiffness of the abutment also changes during the service life of IABs. For example, the stiffness of the concrete abutment decreases due to cracking (Wood and Nash, 2000). Within the above context, it becomes very relevant to improve the understanding of the IAB's behaviour for different stiffness-to-abutment combinations under thermal cyclic loading.

To better assess the performance of IABs within their life cycle, a 1g small-scale instrumented physical model was built in the Structures Laboratory at the University of Bristol (UK) to replicate an IAB backfill under accelerated seasonal expansion and contraction of a bridge deck. The experimental programme specifically investigated the performance of three different bending stiffnesses for the abutment. The experimental data were compared with the results from the numerical models using ABAQUS and PLAXIS. The sensitivity of the stiffness of the abutment, number of loading cycles, loading speed and displacement amplitude of initial cycles is discussed. The simple Mohr-Coulomb numerical models calibrated using the experimental data are suitable for assessing earth pressure build-up for rapid design decision-making in the absence of more advanced SSI modelling. The numerical models also allow for investigation of some of the limitations of the experimental setup to inform further investigation and larger-scale experiments aimed at reducing scaling effects on the results (e.g., Bhattacharya et al., 2021; Liu et al. 2022).

2. Experimental physical model design

The test rig was designed to simulate the effect of the backfill of abutment displacements due to seasonal expansion and contraction of a bridge deck. Measurements included lateral stresses behind the abutment wall using Total Earth Pressure Cells (TEPCs), backfill surface displacement using Linear Variable Differential Transducers (LVDTs) and backfill soil deformation behind the abutment using Particle Image Velocimetry (PIV). The backfill material was loaded by the moving abutment wall with three different bending stiffnesses from flexible to rigid. The displacements replicating horizontal thermal loading conditions were applied as increasing cyclic displacements and multiple-cycle constant-displacement histories.

2.1 Experimental configuration

A test box of 1525 × 1050 × 1150 mm^3 accommodated the loading system and 1000 × 1000 × 960 mm^3 specimen of backfill. A 1000 mm high moveable wall was hinged at the bottom of the soil box to simulate an integral bridge abutment able to rotate about its base, with loading applied via an actuator at 870 mm height. Three moveable wall configurations were tested (Table1, Figure 1b): type S1 - a multi-layer wall made of 25 mm thick Perspex and 25 mm thick timber composite layer to simulate a flexible abutment wall (already presented in Luo et al. 2022), type S2 - a single Polyethylene (PE500) layer 100 mm thick, and finally type S3 - comprising 25 mm Perspex, 25 mm timber composite, 40 mm aluminium frame and 25 mm timber composite producing a sandwich configuration. The hinge of the moveable wall is realised in two ways. In S1 and S3, the hinge is a fixed timber beam to stop the moveable wall from moving further (away from the backfill) and on the other side of the moveable wall, the backfill prevents the moveable wall from moving further (push into the backfill). The other type (in S2) still has a fixed timber behind the moveable wall but has also a steel tube fixed at the end of the wall, which smoothens the movement of the end wall and was created given the change of wall thickness and material (Figure 1b). The Perspex (Carville, 2023) had a density of 1190 kg/m^3, Young's Modulus of 1200 MP and Poisson's ratio of 0.40. The Aluminium (Rees, 2009) had a density of 2.7 Mg/m^3, a Young's Modulus of 69000 MPa and a Poisson's ratio of 0.32. Timber (Sonelastic, 2023) had a density of 0.45 Mg/m^3, Young's Modulus of 800 MPa and Poisson's ratio of 0.20. PE500 (Ensinger, 2023) had a density of 0.95 Mg/m^3, Young's Modulus of 1100 MPa and Poisson's ratio of 0.42. Perspex was used for the box wall to enable PIV observations of backfill displacements, while the remainder of the rig was designed without metal components to facilitate the use of ground penetrating radar as a monitoring tool (see Figure 1a) whose results are not presented herein. The bending stiffnesses of the three moveable walls are listed in Table 1, where the elastic modulus of S1 is the equivalent elastic modulus of the two layers. In terms of the elastic modulus of S3, the stiffness of the aluminium frame was computed as a layer with the same width and characterised by the equivalent second moment of area of the whole section. The wall flexibility parameter, later determined as *Log* $[\gamma_s \cdot \rho]$ (Rowe, 1952), indicates that S1 should behave as a flexible wall, while S2 and S3 can be categorised as stiff. The abutment wall, end wall and side wall were instrumented with pressure cells, while LVDTs were used to measure the moveable wall displacement and the surface backfill displacements. The rig represents a 1-g small-scale setup with scaling implications needing specific discussion. This aspect is addressed later in the manuscript, where the results are discussed (Bhattacharya et al., 2021).

Table 1. Stiffness properties of moveable walls S1, S2 and S3

Moveable /Abutment Wall ID	**Elastic modulus, E, (MPa)**	**A (mm^2)**	**I (mm^4)**	**EI (N*mm^2)**	$\rho *= H^4/EI$ (m^3/kN)	$L_m = H(E_s/EI)^{**}$
S1	1000	5.00E+04	1.05E+07	1.05E+10	809E-4	18.3E-10
S2	1100	1.00E+05	8.30E+07	9.13E+10	93.0E-4	2.10E-10
S3	23491	1.12E+05	11.8E+07	277E+10	3.06E-4	0.07E-10

*Rowe (1952); **mechanical length considering SSI (e.g., Anoyatis et al. 2013), where E_s = 20MPa is the Elastic Modulus of the soil (see Table 5).

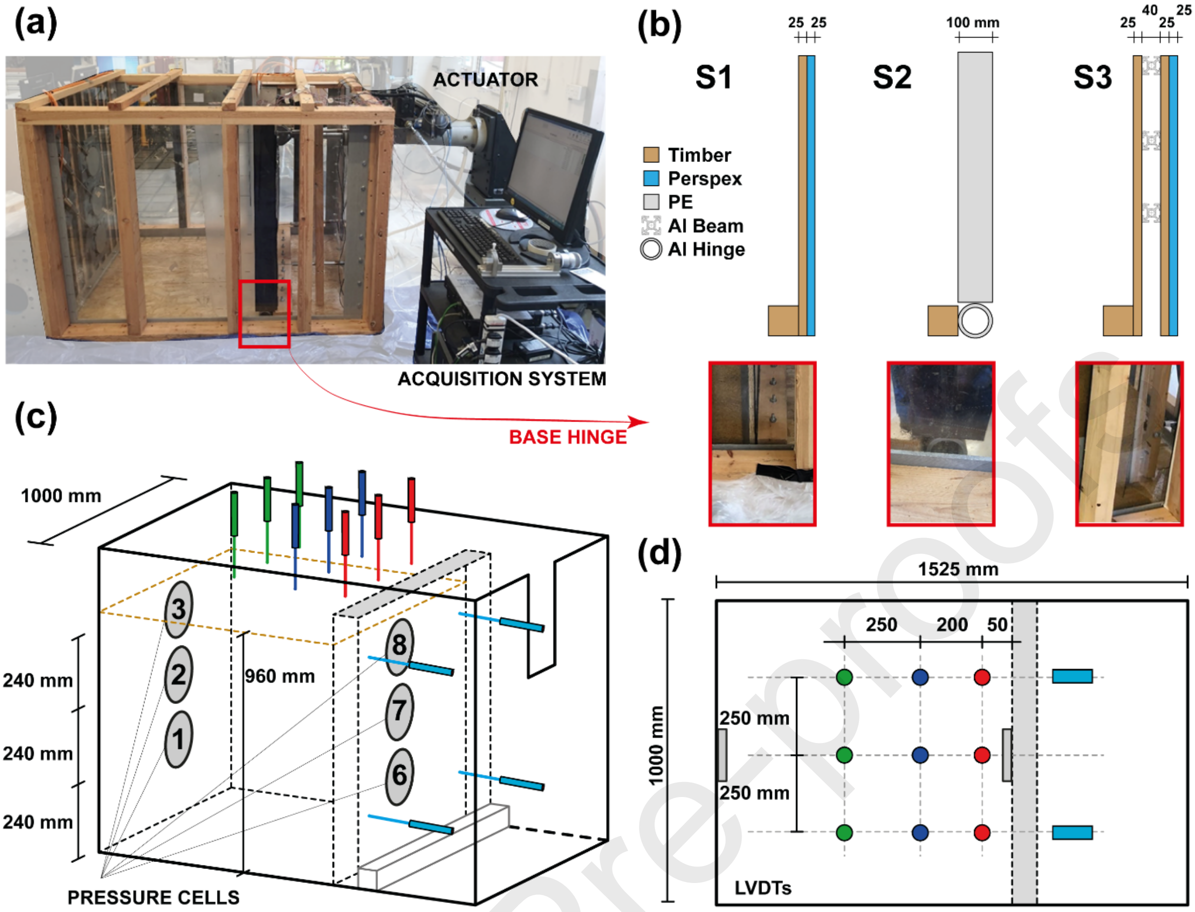

Figure 1. (a) Photo of experimental setup including actuator and acquisition system; (b) section and size of the wall with S1, S2 and S3 stiffness; (c) location of pressure cells on the end of the wall (1-3) and moveable wall (6-8) and LVDTs; (d) top view of the test box identifying LVDT positions.

2.2 Instrumentation layout

The instrumentation consisted of TPC-4000 series TEPCs to measure lateral pressures, LVDTs and a high-resolution camera on the side of the test rig to measure displacement fields in the backfill. The TEPCs measure total pressure (combined effective and pore water pressure) in soils. As the sand backfill was dry, they directly provided effective stress measurements. Figure 1 shows the locations of the TEPCs for the moveable wall, the end wall and the side walls, respectively.

Figure 1 shows the positions of the nine LVDTs (1-9) placed in three rows on the backfill surface (only applied in the first test, #S1-I-12, see Table 2) and four LVDTs (11-13) measuring the moveable (abutment) wall displacement present in all tests. The high-resolution camera (Canon 70D 5472×3648 pixels) focused on the Perspex sidewall to record a 'full field' backfill deformation field using the PIV method, regarded as slow 'fluid motion' (Stanier et al., 2015).

2.3 Thermal loading

Thermal loading from temperature-induced cyclic expansion and contraction of the bridge deck was simulated by a push-pull pseudo-static motion of the moveable wall, its displacement being controlled by the actuator mounted 870 mm above the wall base. Seasonal thermal loading on integral bridges represents the cyclic load caused by the contraction and expansions of the deck, which is monotonically linked to the change of temperatures during winter and summer. In PD6694 (2011), this seasonal thermal loading is modelled through an imposed displacement on the top of the bridge support (abutment), which is calculated as:

$$d = \alpha L_X (T_{e;max} - T_{e;min}) \quad (1)$$

Where:

α is the coefficient of thermal expansion of the deck;

L_X is the expansion length measured from the end of the bridge to the position on the deck that remains stationary when the bridge expands;

$T_{e;max}$ and $T_{e;min}$ are the characteristic maximum and minimum uniform bridge temperature components for a 50-year return period given in the UK (National Annex to BS EN 1991-1-5, 2003).

Two sets of loading protocols were considered, one with increasing displacements per cycle (I) and one with constant displacement at each cycle (C). A maximum displacement of 30 mm was adopted in all tests corresponding to a drift of 3.45%, calculated as displacement over the height of the actuator load cell (d = 30/870). This was employed as a limit and extreme value to assess the effect of significant drifts on the backfill. This is higher than the typical order of magnitude of drift due to seasonal deck movement (one end) of an IAB in London with a 150 m long concrete deck or a 100 m long steel deck and an abutment wall height of about 5m, which is ~0.6% (England et al. 2000). It is worth noting that the above drift value should not be viewed as pure engineering shear strain, as the drift also includes rotation, and it is correlated with shear strain (Bolton and Powrie 1987). Tests are identified by the stiffness of the wall (S1, S2 or S3), the type of loading (increasing or constant, I or C) and the number of cycles (see Table 2). In Test #S1-I-12, the flexible abutment wall S1 was subjected to 12 loading cycles with a loading rate of 0.5 mm/s (Springman et al., 1996; Lehane, 2011), each cycle lasting at least 40 seconds. The cyclic displacements at the top of the moveable wall started at ±5 mm, with increments of ±5 mm every two cycles, to reach ± 30 mm (drift ~3.45%; see Table 2). In Test #S2-I-5, the rigid abutment wall S2 was subjected to the same loading velocity as the first five cycles of Test #S1-I-12 (0.5 mm/s) and the same amplitude, stopping the test at cycle 5. In Test #S2-I-12, the rigid abutment wall S2 was then subjected to the same loading amplitude as Test #S1-I-12, with a loading rate of 1 mm/s (i.e., same loading protocol, different stiffness and load velocity).

In Test #S2-C-5, the rigid abutment wall S2 was subjected to 5 cycles with a loading rate of 1mm/s and a constant amplitude of 30 mm. Finally, in Test #S3-C-5, the abutment wall S3 was subjected to 5 cycles with a loading rate of 1 mm/s and cyclic displacements at the top of the wall fixed at ±30 mm for each cycle (1 mm/s was considered slow enough to simulate static thermal loading, England et al. 2000). All test IDs and their characteristics are summarised in Table 2.

Table 2. Summary of experimental parameters for the different test configurations.

Test ID	Movable Wall	Total Cycles	Cycle Loading		Loading Rate [mm/s]
#S1-I-12	S1	12	Displacement (mm)	$2 \cdot \{\pm 5; \pm 10; \pm 15; \pm 20; \pm 25; \pm 30\}$	0.5
			*Equivalent Drift (%)**	$2 \cdot \{\pm 0.57; \pm 1.15; \pm 1.72; \pm 2.3; \pm 2.87; \pm 3.45\}$	

#S2-I-5	S2	5	Displacement (mm)	$2 \cdot \pm 5; 2 \cdot \pm 10; \pm 15$	0.5
			Equivalent Drift (%)	$2 \cdot \pm 0.57; 2 \cdot \pm 1.15; \pm 1.72$	
#S2-I-12	S2	12	Displacement (mm)	$2 \cdot \{\pm 5; \pm 10; \pm 15; \pm 20; \pm 25; \pm 30\}$	1
			Equivalent Drift (%)	$2 \cdot \{\pm 0.57; \pm 1.15; \pm 1.72; \pm 2.3; \pm 2.87; \pm 3.45\}$	
#S2-C-5	S2	5	Displacement (mm)	$5 \cdot \{\pm 30\}$	1
			Equivalent Drift (%)	$5 \cdot \{\pm 3.45\}$	
#S3-C-5	S3	5	Displacement (mm)	$5 \cdot \{\pm 30\}$	1
			Equivalent Drift (%)	$5 \cdot \{\pm 3.45\}$	

*Equivalent drift is defined as displacement (monitored by actuator load cell) divided by actuator height (870mm)

This study explored the potential effects of the abutment bending stiffness, with bridge span lengths beyond the design code guidance (60 m), to see the possible performance of a large-span integral bridge under thermal loading. In this experimental campaign, most of the tests were loaded by less than 12 cycles to assess the rapidly increasing pressure along the abutment wall appearing in the first 10 cycles (i.e., 10 years of service for an integral bridge England et al., 2000), but also accounting for significantly higher drifts with respect to those characteristics of IABs monitored in the field.

2.4 Backfill

The backfill material selected was Leighton Buzzard Sand (LBS) fraction B (Lings and Dietz, 2004; Kloukinas et al., 2015; Fiorentino et al., 2021). The LBS's minimum and maximum dry densities were assumed as 1.48 Mg/m^3 and 1.65 Mg/m^3; see Fiorentino et al. (2021). The specific gravity of LBS grains was assumed to be 2.65, while the minimum and maximum void ratios (e_{min} and e_{max}), were 0.64 and 0.83, respectively (Fiorentino et al., 2021).

The average dry densities achieved in each test ID ranged from 1.44 Mg/m^3 to 1.51 Mg/m^3 (Table 3). The density values obtained in Tests S2 and S3 were slightly lower than the aforementioned minimum value provided by Fiorentino et al. (2021), but the difference is within acceptable limits considering that the density calculated and reported in Table 3 is the average on all rigs and the test was meant to start from a non-compacted condition. To achieve a uniform and relatively loose LBS specimen, the sand was pluviated into the soil box in three layers, with levelling (but no compaction). The only exception was test #S2-C-5, where minimum compaction (gentle manual pressure) was applied on the last layer for levelling purposes.

Table 3. Summary information of the backfill in each Test configuration.

Test ID	*#S1-I-12*	*#S2-I-5*	*#S2-I-12*	*#S2-C-5*	*#S3-C-5*
Dry density (Mg/m³)	*1.48*	*1.49*	*1.46*	*1.51*	*1.44*
Density ratio with respect to Test #S1-I-12	*100%*	*100.7%*	*98.6%*	*102.0%*	*97.3%*
*Wall flexibility Log [$\gamma_s \cdot \rho$]**	*3.14*	*2.16*	*2.16*	*2.17*	*0.71*

*Rowe (1952): ρ is defined in Table 1 and γ_s is the soil dry unit weight (equal to the dry density reported in the table times g = 9.81m/s²).

3. Results & discussion of experimental data

This section discusses the effect of the abutment stiffness, the loading speed, and the amplitude on the backfill pressure build-up. Figure 2 shows the force-displacement responses of the actuator for four of the different test configurations. The actuator force was normalised by $\gamma_s H^2 L$, being H the original soil depth and L is the width of the backfill and γ_s the solid dry density, and drift is calculated as in Table 2. To achieve the same displacement of the wall towards the soil, the actuator had to impose a larger force with increasing cycles. This is likely due to the densification of the soil, increasing particle interlocking and soil strength. The tests with stiffer moveable walls reached a larger actuator loading overall (see Figure 2a). In the case of #S3-C-5 (Figure 2b), this is true just for the first two cycles, and then the hierarchy changes since a process of delamination of the sandwich section is initiated (see section 3.4 for further details on this aspect of test #S3-C-5).

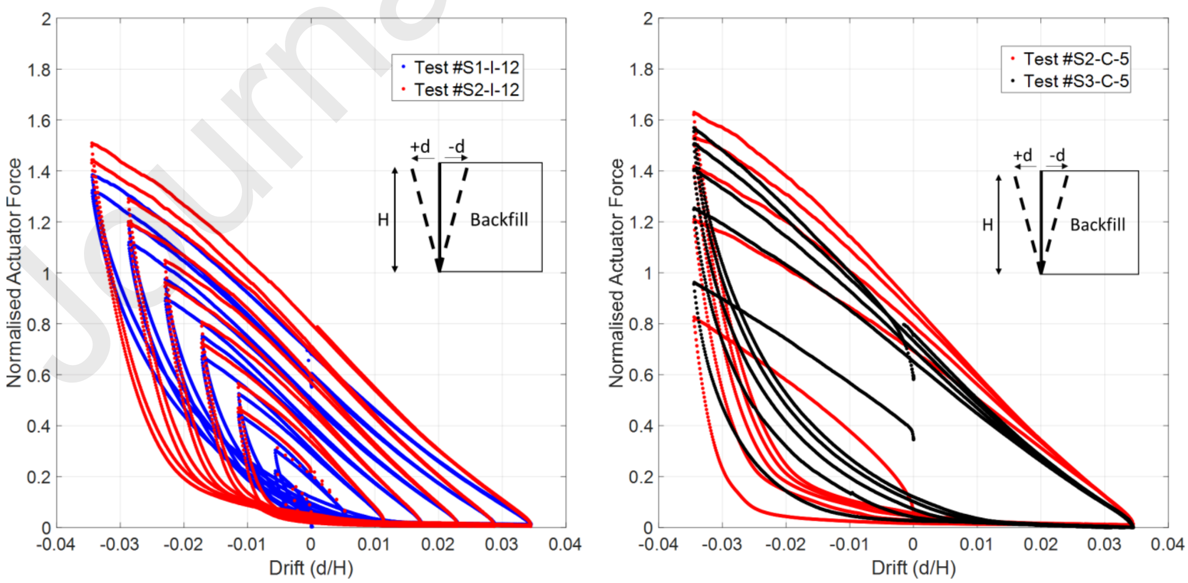

(a) *(b)*

Figure 2. Normalised actuator force (by $\gamma H^2 L$) vs wall drift (d/H) for (a) increasing amplitude tests (i.e., #S1-I-12 (blue) and #S2-I-12 (red)) and (b) constant large amplitude tests, i.e., #S2-C-5 (red) and #S3-C-5 (black).

Figure 3 shows the lateral pressure measured by pressure cell #7 at the middle position of the movable wall in test #S1-I-12, with the comparison of the horizontal actuator movement. The lateral pressure reached peaks when the actuator reached the maximum push towards the backfill (passive state position). In contrast, the pressure decreases to the minimum value when the actuator has the maximum retraction from the backfill (active state position). The lateral pressure in the passive state increases rapidly with increasing cycles, while in the active state, it slightly increases. Both trends reflect an increase in soil friction angle due to the greater soil density and particle interlocking that occur with an increasing number of cycles. The active state is reached as soon as the actuator movement reaches zero displacement (or even somewhat earlier), as evident from the plateau in active pressures. On the other hand, the passive resistance is not fully mobilised as it increases monotonically with actuator movement without reaching a plateau. According to the PIV analysis from Luo et al. (2022), the amplitude of the backfill densification decreases with increasing loading cycles in the same test.

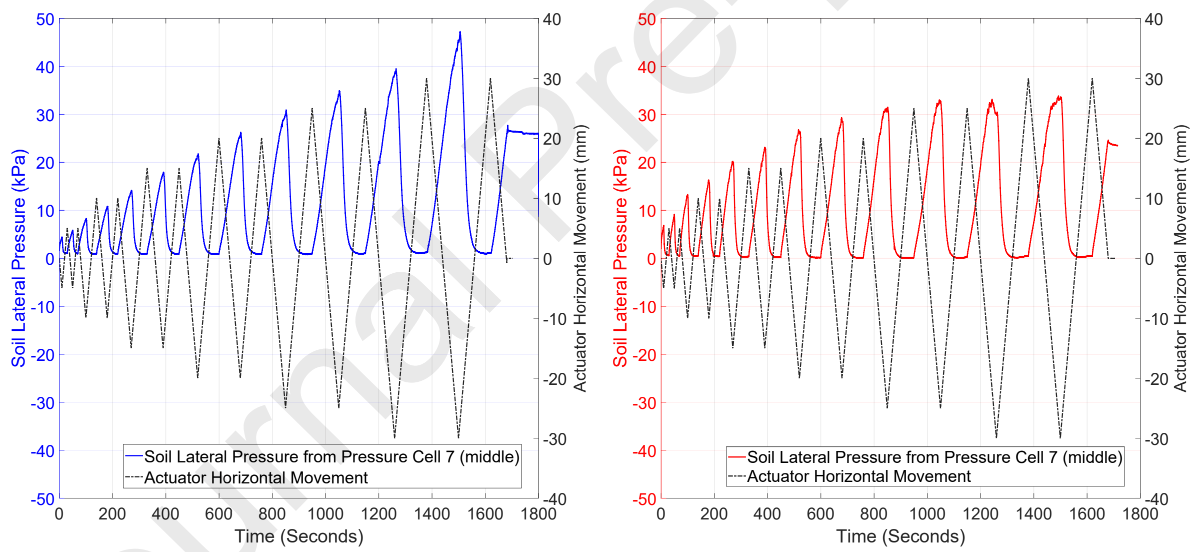

(a) (b)

Figure 3. Lateral pressure at the middle of the moveable wall versus horizontal actuator movement as a function of time in (a) Test#S1-I-12 (“flexible wall” as per Table 3) (b) Test#S2-I-12 (“stiff wall” as per Table 3).

The settlement of the backfill surface was measured by LVDTs, and a camera was located on the side of the box, with Figure 4 showing the results of the first three cycles of test #S1-I-12. The settlement measured by the camera has a systematic offset of 5 mm, which becomes relatively small in the case of larger cycles when LVDTs are lost due to the settlement exceeding the maximum LVDT measure. The 5 mm offset is likely caused by a systematic offset in the video estimation. For comparison purposes between Test IDs, the difference does not affect the conclusions.

The effect of the loading speed on the results obtained can be checked by comparing test #S2-I-5 and the first five cycles in test #S2-I-12. The lateral earth pressure measured in test #S2-I-12 (higher loading speed) is slightly larger than that in test #S2-I-5. This may be due to the low compaction level of the backfill. The difference between the two tests decreased with increasing loading cycles. The testing speed does not affect the results significantly, and both velocities can be considered suitable for the pseudo-static assumption (England et al., 2000). A visual comparison of the settlement accumulated in the first ten cycles of S1-I-12 is shown by comparing Figures 4c, 4d and 4e.

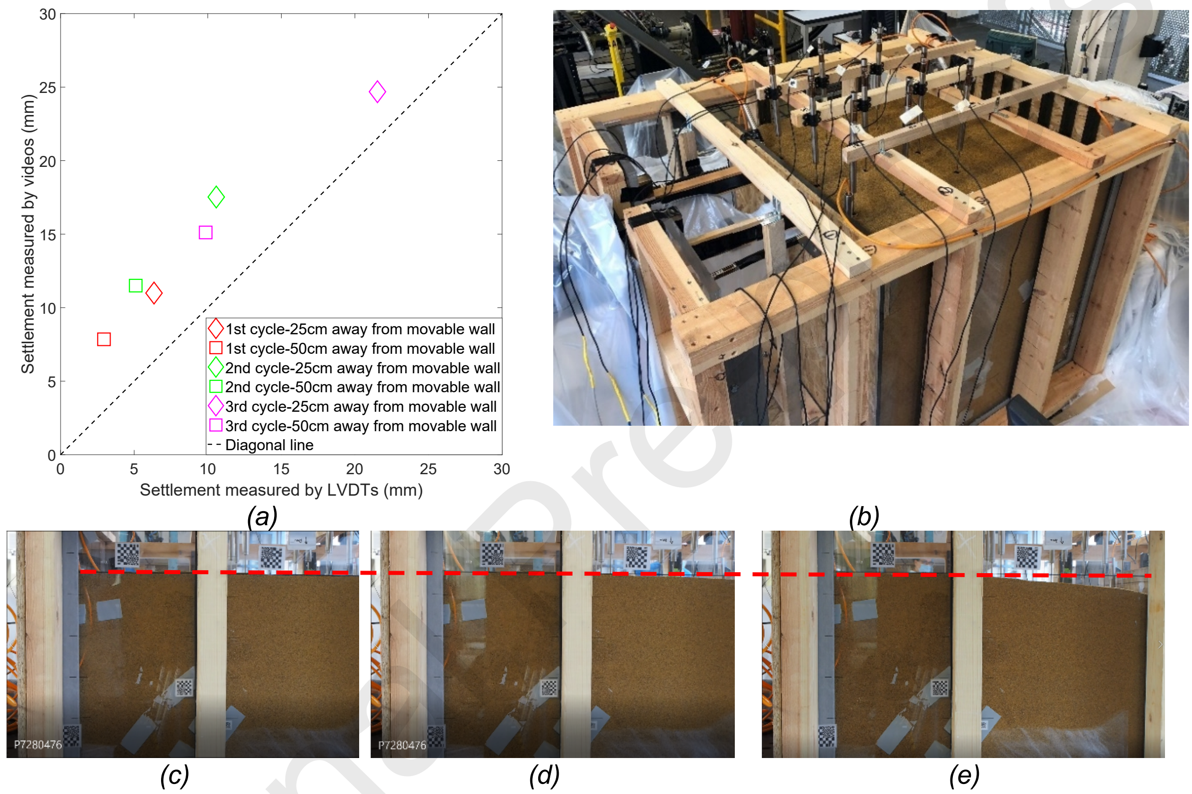

Figure 4. (a) Settlements measured by the LVDTs versus settlements obtained from video recordings in Test #S1-I-12, (b) photo of #S1-I-12 test at the initial state with LVDTs. Photo of settlement for #S1-I-12 test (c) before the test, (d) after 2 cycles and (e) after 10 cycles.

3.1 Effect of the abutment stiffness with increasing displacement amplitude

Figure 5 shows the experimental results of the three pressure cells at the discrete levels of 240, 480, and 720 mm above the base of the moveable wall (pressure cells #6, #7, and #8, as shown in Figure 1) and how the maximum pressures increase throughout the cycles. They seem to increase exponentially as the cycles and displacement increase. In the first cycle, the passive pressures start approximately at the same value for each sensor, but they increase at different rates, with the middle sensor having the fastest rate of increase. This could be due to the dual effect of earth pressure increasing along the height of the wall according to the to the passive pressure trend suggested in PD6694 (Denton et al., 2011) but also to the different pressure distribution caused by the deformation of the wall changing for different tests (i.e., S1 versus S2)

In general, the soil pressure seems to have a steadily increasing trend, which may be expected since the actuator displacement increased linearly. With the increasing number of cycles, the lateral earth pressure (Figure 5) and total actuator loading (Figure 2) also increased. The relationship between the cycle number and the lateral earth pressure was non-linear, with a decreasing growth rate. These results agree with the study of Walter et al. (2018). When comparing test #S1-I-12 with test #S2-I-12 to investigate the effect of the abutment stiffness, it was found that the pressure envelope shape along the moveable wall was similar. The peak lateral earth pressure measured along the stiffer moveable wall (#S2-I-12) is approximately 10% higher than that for, the less stiff wall (#S1-I-12). The incremental increase in earth pressures steadily declines with the number of loading cycles in all the tests (England et al., 2000). However, the rate decreases more rapidly in the tests with a stiffer moveable wall. The maximum ratio of horizontal to vertical stress (Figure 5b) occurs close to the surface of the backfill, while the minimum value is found at the bottom of the moveable wall. As noted above, the bending stiffness of the abutment wall does not have a major influence on the ratio of the horizontal to vertical stresses (*K*). The magnitude of *K* is discussed later in relation to the boundary condition of the rig (see section 3.4).

As mentioned in the previous section, a camera was set up on one side of the box during the tests. Based on these videos, the settlement of the backfill surface of test #S1-I-12 (flexible wall) and test #S2-I-12 (stiffer wall) are plotted in Figure 6a. The settlement at a distance of 200 mm from the moveable wall has been recorded over the loading cycles of the five tests and is presented in Figure 6b. The settlement developed steadily with the increasing number of cycles. Although a reduction in the settlement per cycle was observed, there was no indication that an asymptotic value of the settlement was ever approached. The test with a stiff moveable wall seems to have greater soil settlement, especially in the initial few cycles. The initially loose sand used in the test means that the settlement measurements are not fully indicative of a typical field condition, where the backfill would be well compacted.

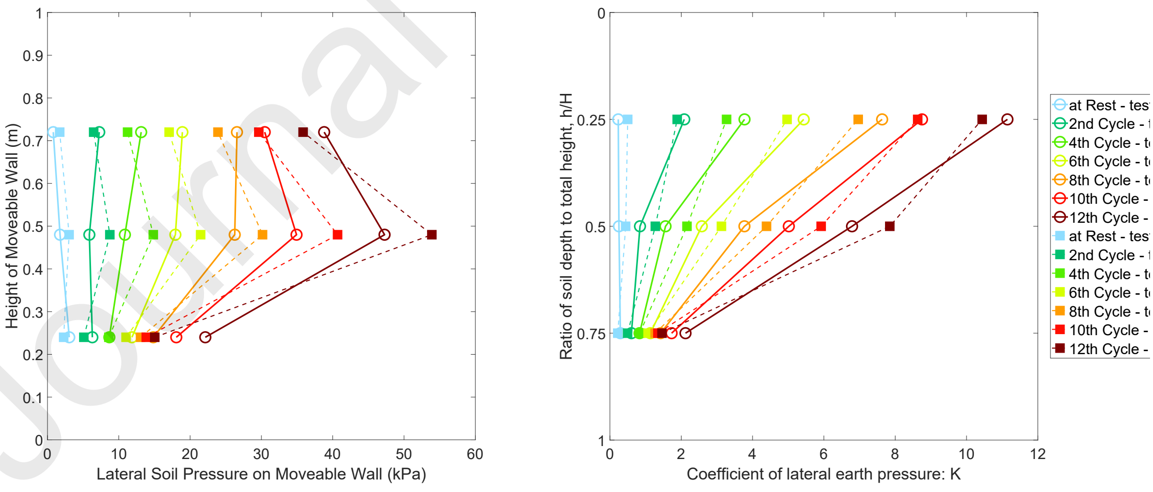

(b)

(a)

Figure 5. (a) Lateral earth pressure (passive state – push toward backfill) on the moveable wall at pressure cells 6, 7 and 8 (see Figure 1) and (b) Coefficient of lateral earth pressure (K).

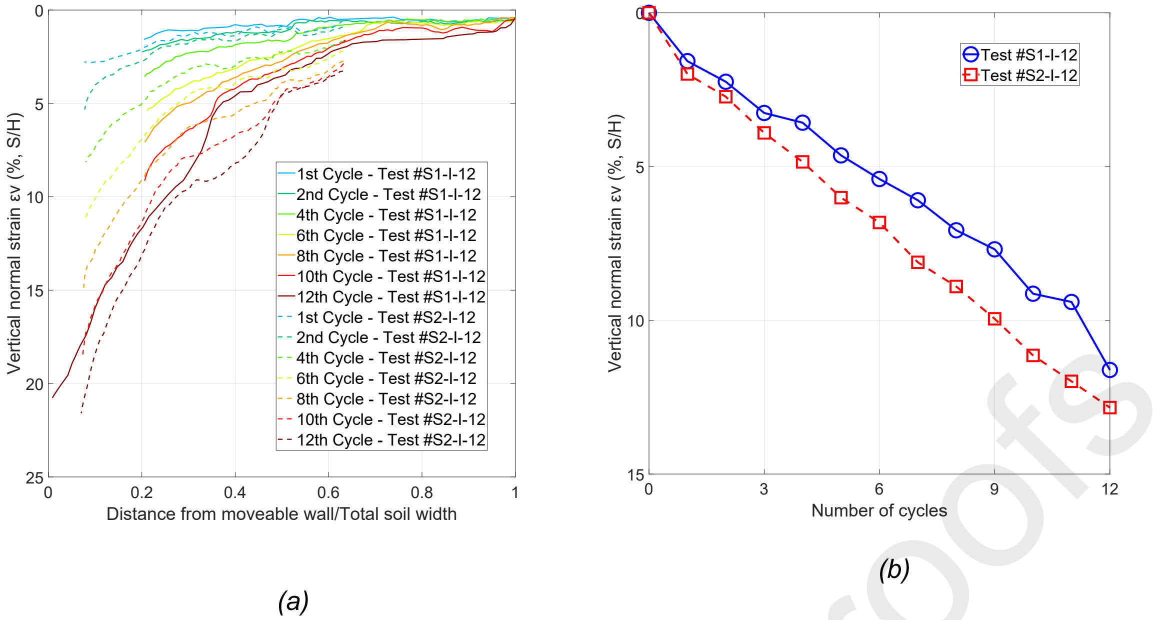

Figure 6. (a) Settlement (S) of the backfill surface in test #S1-I-12 and #S2-I-12; (b) Settlement at 200 mm distance from the moveable wall with cycles for test #S1-I-12 and #S2-I-12 captured through a high-resolution camera (settlements are captured at the end of each cycle when the wall is back to vertical position).

3.2 Effect of the abutment stiffness with constant displacement amplitude

Figure 7a presents *K* along the depth of the two tests with constant loading (i.e., #S2-C-5 and #S3-C-5). In both tests, the wall can be taken as rigid based on flexibility estimated in Table 3. Therefore, there is not much difference in the lateral soil pressure in the first few cycles. Given the limited number of monitored cycles, this cannot necessarily be extended to more cycles (e.g., the entire life of a bridge).

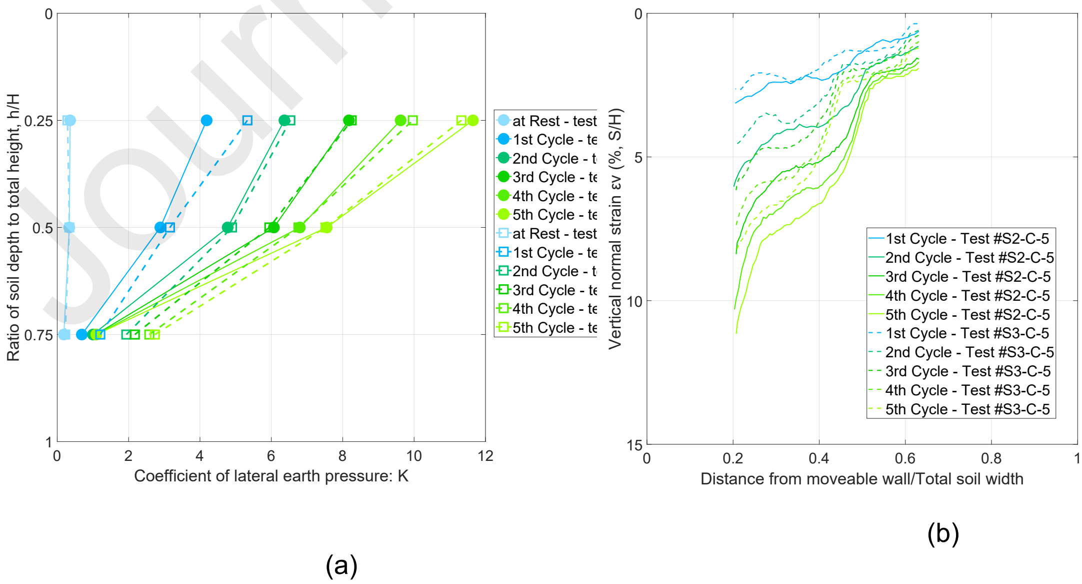

Figure 7. (a) Coefficient of lateral earth pressure (K) on the moveable wall (in the maximum passive state) and (b) settlement of backfill surface for tests #S2-C-5 and #S3-C-5.

In test #S3-C-5, the lateral pressures at the top and middle positions were less than in test #S2-C-5, and the difference increased with the number of loading cycles. In contrast, the lateral pressure at the bottom position was higher than that in test #S2-C-5. The pressure data for S2 and S3 cases started to overlap in the last two cycles. The moveable wall in S3 had a continued slight drop in stiffness due to the initiation of delamination in the sandwich section, which increased with the number of cycles. This phenomenon could be the cause of the pressure overlap in cycles 4 and 5 (see Figure 7a). While not desirable in a controlled model test, this effect could be realistic, as a concrete abutment may reduce in stiffness with the development of concrete cracking over the life cycle of the bridge.

Figure 7b shows the settlement curves of the two tests. Test #S2-C-5 has larger settlements than #S3-C-5. The difference is not very significant and may be caused by the difference in wall stiffnesses and also to the higher level of compaction of #S2-C-5 (see Table 3), preventing the decoupling of the two effects.

3.3 Analytical and empirical expressions of the ratio of horizontal to vertical stresses

In the design guidance for IAB's, the critical parameter is the ratio of the horizontal to vertical soil stresses acting behind the bridge abutment (*K*), which is determined through different formulations in each of the design guidelines (see Table 4). In Figure 8, the analytical and empirical equations considering the horizontal movement are presented together with the Coulomb passive earth pressure coefficient which considers the soil-wall friction but not the horizontal movement, (Powrie 2004). Coulomb passive earth pressure coefficient is reported in Equation 2 (Coulomb 1776):

$$K_{P,Coulomb} = \frac{\sin{(\alpha - \emptyset)}^2}{\sin{\alpha}^2 \sin{(\alpha + \delta)}[1 - \sqrt{\frac{\sin{(\emptyset + \delta)}\sin{(\emptyset + \beta)}}{\sin{(\alpha + \delta)}\sin{(\alpha + \beta)}}}]^2} \qquad (2)$$

Where

$\emptyset$ is internal friction angle of the soil,

β is the slope of the backfill,

α is the angle of the back of retaining wall,

δ is friction angle between soil and back of retaining wall assumed as $2/3\phi$.

In our study, $\emptyset = 32, \beta = 0, \alpha = 90$, when $\delta = 0, K_p = 3.255$; while $\delta = 22, K_p = 7.574$. Figure 8 shows *K* estimated from the readings of the middle (h/H=0.50) and top cells (h/H=0.25) in each cycle of the five tests compared with analytical and empirical K estimations. The tests are divided into two groups: increasing loads: #S1-I-12, #S2-I-5 (Figure 8a 8c), and #S2-I-12 and constant loads: #S2-C-5 and #S3-C-5 (Figure 8b 8d). Tests with the same loading amplitude show similar trends in pressure build-up. As shown in Figure 8a, the *K* value determined from the experiments at the middle position is beyond the guidance value from the Massachusetts Bridge Manual (1999) after 11 cycles in #S1-I-12 and #S2-I-12. The *K* value determined from the experiments exceeds PD6694 (2011) after four cycles in #S2-I-5 and #S2-I-12 and six cycles in #S1-I-12.

In the test group with constant large loading amplitude, the experimental *K* at the middle position is higher than the value suggested by the Massachusetts Bridge Manual (1999) after the first three cycles, and immediately after the first cycle the values proposed in the PD 6694 (2011), Barker et al. (1991) and Navfac (1982) are exceeded as well. The differences between the predictions of the empirical and analytical formulae and the measurements in the campaign at hand could be attributed to the differences in material properties of the backfill and the boundary conditions at the top and the bottom of the wall. The Coulomb theory estimation is affected significantly by the wall friction that, when assumed equal to $2/3\phi$, provides a satisfactory estimation of the earth pressure but is still not suitable for all cases evidencing the need for a more accurate analytical formulation (e.g., Mylonakis et al 2007, Huang et al. 2022). The value of the friction angle assumed for the estimation of analytical models in Table 4 is 32 degrees reflecting the loose backfill condition (Sadrekarimi & Olson, 2009).

Table 4. Analytical formulations for the estimation of K in IABs depending on displacement

$K = 0.43 + 5.7\left[1 - e^{-190\left(\frac{d}{H}\right)}\right]$	*Massachusetts Bridge Manual, 1999*
$K = K_0 + 28\left(\frac{d}{H}\right)^{0.33}$	*Dicleli and Albhaisi, 2004b*
$K_d^* = K_0 + \left(\frac{Cd'_d}{H}\right)^{0.6} K_{p;t}$	*PD 6694-1 (BSI, 2011)*
$K = K_0 + \emptyset\, d \le K_p$	*Bal et al., 2018*

Where d is the displacement of the IB towards the backfill soil; H is the height of the abutment; K_0 is the at-rest earth pressure coefficient; d'_d is the wall deflection at depth $H/2$ below ground level; C is a dimensionless coefficient equal to 20 for foundations on loose soils with Young's modulus $E \le$ 100 MPa, and 66 for foundations on rock or soils with $E \ge$ 1000 MPa, and which may be determined by linear interpolation for values of between 100 MPa and 1000 MPa; $K_{p;t}$ is the coefficient of passive earth pressure used in the calculation of K_d^*; $\emptyset$ is the slope of the earth pressure variation with horizontal displacement (which varies with backfill type); K_p is the passive earth pressure coefficient given by the Rankine theory equal to $(1 - sin\phi)/(1 + \sin\phi)$ where ϕ is the friction angle.

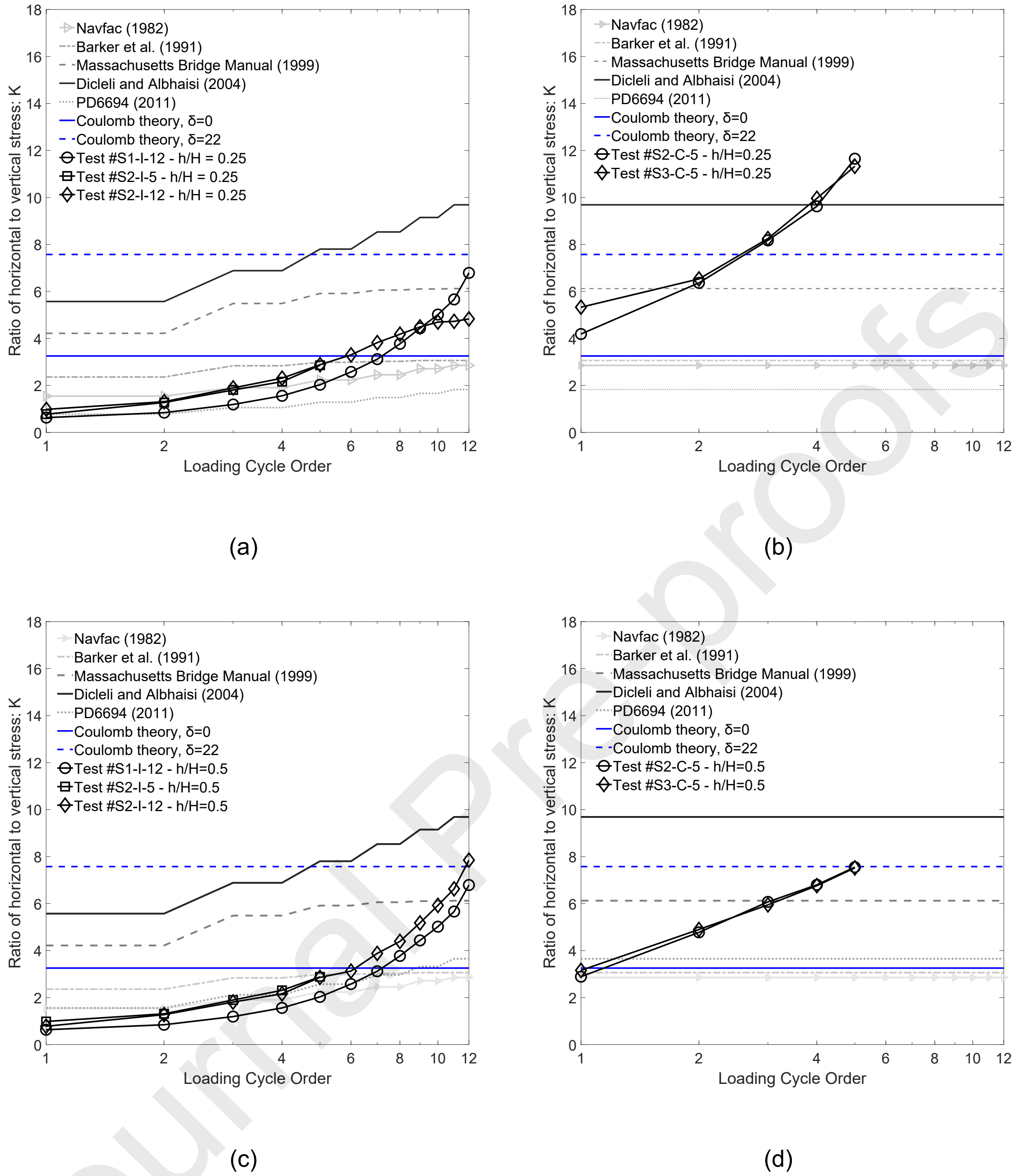

Figure 8. Experimental trends for K at different wall positions in case of tests with (a) increasing (h/H=0.25) and (b) constant displacement amplitude with number of cycles (h/H=0.25) (c) increasing (h/H=0.50) and (d) constant displacement amplitude with number of cycles (h/H=0.50) compared with analytical (Massachusetts Bridge Manual 1999; Dicleli and Albhaisi 2004b; PD6694 2011 and Coulomb 1776) and empirical (Navfac 1982 and Barker et al. 1991) formulations provided in guidelines estimated assuming ϕ = 32 degrees and H = 870 mm.

3.4 Effect of test rig size

The end wall experiences significantly less pressure than the moveable wall. The *K* value along the end wall is presented in Figure 9. It was found that the *K* value increased with the number of cycles and consistently above the K_0 value of 0.47 (according to Jaky's theory assuming $\varphi = 32\ degrees$) in this study. The development of the full passive wedge was limited due to the size of the rig, and an extended soil box would have been required for its full development. Therefore, the end wall may contribute an additional passive pressure on the moveable wall affecting the comparison shown in section 3.3. The *K* value at the top position experiences a noticeably higher value than the others on the end wall, especially in the stiffer moveable wall test (#S3-C-5). This is likely due to the top pressure cell at the back wall being located within the theoretical passive wedge, while the two others are not (see Figure 9b). The comparison of Figure 9a and 9b also indicates that the failure wedge length increases with the increase in the stiffness of the abutment. The numerical analyses presented in the following section are used to assess the effect of this boundary condition on pressures.

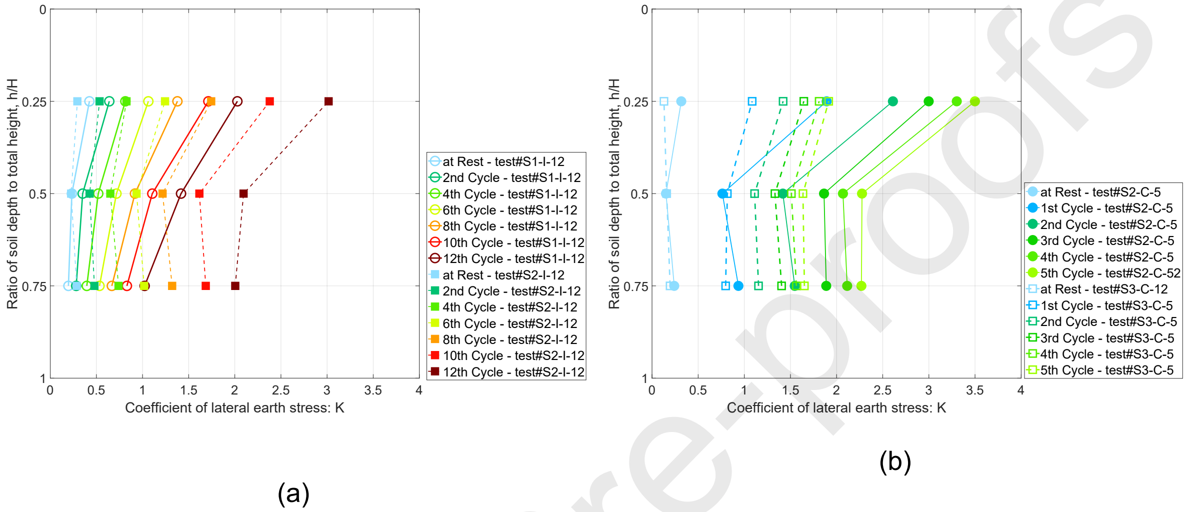

Figure 9. Coefficient of passive-like lateral earth pressure (K) on the end wall for (a) increasing amplitude (#S1-I-12 and #S2-I-12) and (b) constant large amplitude (#S2-C-5 versus #S3-C-5) tests.

4. Numerical Analyses

To investigate the behaviour of IABs under seasonal thermal loading, the experimental campaign was also modelled numerically in ABAQUS (Khodair and Hassiotis, 2005; Sadrekarimi and Olson, 2009) and PLAXIS (Sandberg et al., 2020; Silva et al. 2023) using a simplified Mohr-Coulomb constitutive model. This modelling allowed an initial assessment of the influence of different abutment stiffnesses and the effect of boundary conditions in the test rig on the results. The comparison also provides useful information on the suitability of different software packages for rapid assessment of SSI for design purposes, highlighting where different assumptions might be needed, notwithstanding the purpose of using the same model.

4.1 Finite Element Modelling

The parameters of the Leighton Buzzard Sand model are based on triaxial compression tests of Ottawa quartz sand (Sadrekarimi and Olson, 2009). The backfill soil (LBS) is defined by a Mohr-Coulomb model. For loose contractive sands (which initially lie above the critical state line), the mobilised friction angle becomes approximately equal to the critical state friction angle; thus, there is no negative or positive dilatancy angle (Manzari and Dafalias 1997; Been and Jefferies 2004). Still, to ensure the convergence of the model in ABAQUS, a critical state friction angle (32 degrees) with a non-zero dilatancy angle equal to +1 degree and a non-zero cohesion intercept of 1 kPa were employed to model the loose backfill (Sadrekarimi and Olson, 2009; Abdullah and Naggar 2023). For the same reason, in PLAXIS, a non-zero dilatancy angle in accordance with the software manual (PLAXIS Manuals, 2019) and small non-zero cohesion intercept (0.01 kPa) were assumed. The detailed soil material parameters in the present study are summarised in Table 5, and the stiffness properties of the walls are given in Table 1.

Table 5. Soil material parameters for the Mohr-Coulomb constitutive model used in the finite element analyses.

γ_{unsat} (kN/m^3)	γ_{sat} (kN/m^3)	
14.52 - 14.72*	18.85 - 18.97	
Young's modulus (MPa)	Poisson's ratio	
20	0.2	
Friction Angle φ' (◦)	Dilation Angle Ψ (◦)	Effective Cohesion c'_{ref} (kPa)
32	1/2**	1/0.01***

**as per density presented in Table 3*

***dilation angle equal to 1 degree in ABAQUS and 2 degrees in PLAXIS (due to the relationship to the friction angle, which is suggested by PLAXIS Manuals, 2019)*

***non-zero cohesion value for convergence equal to 1 kPa in ABAQUS and 0.01 kPa in PLAXIS*

In the ABAQUS/CAE 2D simulation model, the moveable walls and soil were modelled using shell elements. The moveable wall was modelled as linear isotropic elastic with plane strain boundary conditions that are chosen to minimise container boundary effects on the backfill sand. In the PLAXIS 2D simulation model, the moveable wall was modelled as a rotating plate, with displacements of the plate allowed in both horizontal and vertical directions. The plate was defined to be elastic. To simulate the hinge at the bottom of moveable walls, a fixed point was added at the bottom of the moveable plate, which prevented displacements in both directions while allowing rotation.

The soil at the bottom of the box was modelled to have fixed displacements in both ABAQUS and PLAXIS without modelling the bottom surface of the soil box. The end wall was explicitly modelled in PLAXIS, assuming a rigid surface and considering the interaction between the Perspex back wall surface and soil, as discussed in section 4.2 for test #S1-I-12. In ABAQUS, the end wall was not modelled explicitly, and the back end of the soil was fully fixed.

4.2 Interaction properties

In the ABAQUS model, for test #S1-I-12, the wall was modelled as two layers, one layer of Perspex and one layer of timber. For tests #S2-I-12 and #S2-C-5, the wall was one layer of PE500. The sandwich wall in test #S3-C-5 was modelled as two layers of material instead of the actual four due to convergence issues; one with the properties of Perspex, and the other with the equivalent stiffness of the timber and aluminium sandwich. Tangential and normal interactions at the backfill-wall interfaces were taken into account using the surface-to-surface discretisation method to enforce an overall contact condition (Alqarawi et al., 2016). A finite-sliding formulation was used at these interfaces, which allows any arbitrary motion of the surfaces, including separation, sliding and rotation of surfaces. A hard contact model defines the normal contact pressure over the closure relationship between the wall (master) and the backfill (slave). Tangential interaction between the wall and the backfill is defined using the static-kinetic exponential decay function. The contact defined between the Perspex wall and the soil was taken as frictionless. To prevent any possible separation at the interface between the base of the moveable wall and the soil, tie constraints were added along the baseline of the moveable wall. A geostatic stress field procedure, in which gravity loads are applied, was used as the first step of the analysis to verify that the initial geostatic stress field is in equilibrium with applied loads and boundary conditions.

The soil-wall interface is managed in PLAXIS in a simpler way. In the PLAXIS model, the interface (roughness) coefficient R_{inter} is an interface strength reduction factor that defines the strength and stiffness of the interaction between moveable walls and soil with values ranging from 0 to 1 ($0 < R_{inter} \leq 1$). Therefore, when the interface between the moveable wall and soil is assumed to be rigid, R_{inter} is set to be one as default, indicating that the relative movement between the moveable wall and soil is very limited. When the interface is smoother and of lower strength, a smaller R_{inter} is assigned but at a value greater than zero (the interface cannot be completely smooth), indicating that there is more relative movement between the moveable wall and soil. Generally, in practice, the strength and stiffness of the interface are lower than the surrounding soil. Therefore, the value of R_{inter} should be lower than 1. In the absence of detailed data on the roughness, it can be assumed that R_{inter} is in the order of 2/3 (PLAXIS Manuals, 2019). Potyondy (1961) tested the skin friction between several types of soil and construction materials and suggested a coefficient of 0.54 for the interface between smooth steel and dry sand and a coefficient of 0.76 for the interface between smooth concrete and dry sand. Considering both the PLAXIS Manuals (2019) and the study by Potyondy (1961), the strength reduction R_{inter} is defined as 0.6 for the #S1-I-12 and #S3-C-5 tests (i.e., Perspex-soil interaction) and increased to 0.7 for modelling of the #S2-I-5, #S2-I-12 and #S2-C-5 tests (i.e., PE500-soil interaction). The difference in modelling the interface between the two software packages likely leads to some differences in the numerical results even if from a conceptual point of view the same kind of physical condition is meant to be modelled (i.e., frictionless surface in the case of Perspex soil interaction).

4.3 Lateral earth pressure along the moveable wall

The lateral earth pressure at the maximum extension (passive state) along the moveable wall from the experimental and numerical models in #S1-I-12 and #S2-I-12 (Figure 10), shows that the overlapping profiles from the two numerical models are similar to the value of the 12th cycle from the experimental tests. This is expected, as the Mohr-Coulomb model cannot capture the changes in the soil density at each cycle.

The different wall stiffnesses result in a different distribution of passive pressures, with the two numerical models being able to reasonably capture the trend of the measured pressures for the more flexible wall configuration (i.e., #S1-I-12 in Figure 10a) but missing the trend shown in the experimental results for test #S2-I-12 (see Figure 10b) beyond the second cycle (where high drifts lead to failure of the soil material).

Figure 11 compares the lateral earth pressure along the moveable wall determined from the experimental and numerical models for #S2-C-5 and #S3-C-5 and shows the inability of the Mohr-Coulomb model to capture the cyclic soil densification in the experiments, giving a steady profile with depth. From the very early cycles, the high value of drift leads to soil failure and to an inaccurate estimation of the pressure distribution with respect to the experimental results.

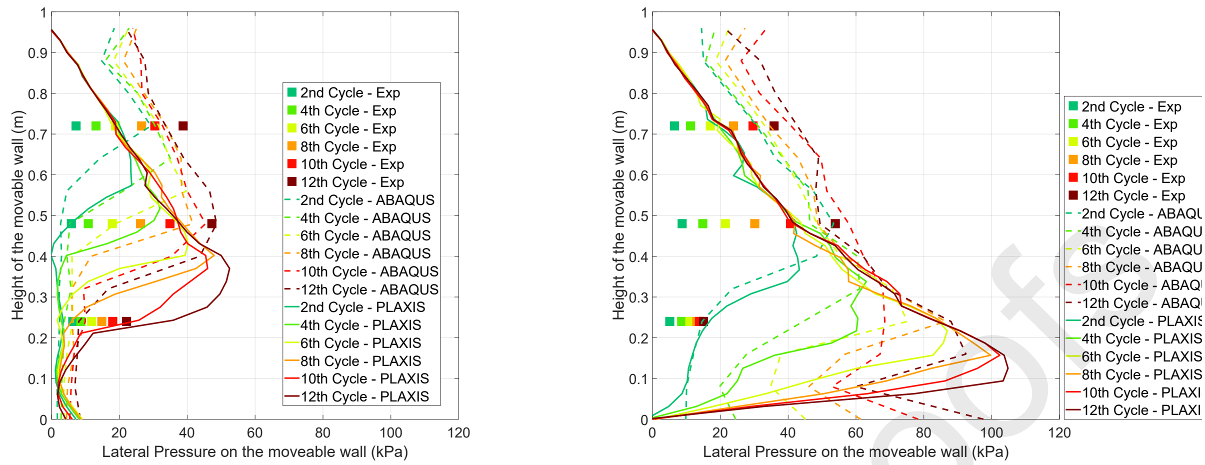

(a) (b)

Figure 10. Lateral earth pressure at the passive stage behind the moveable wall for test (a) #S1-I-12; (b) #S2-I-12.

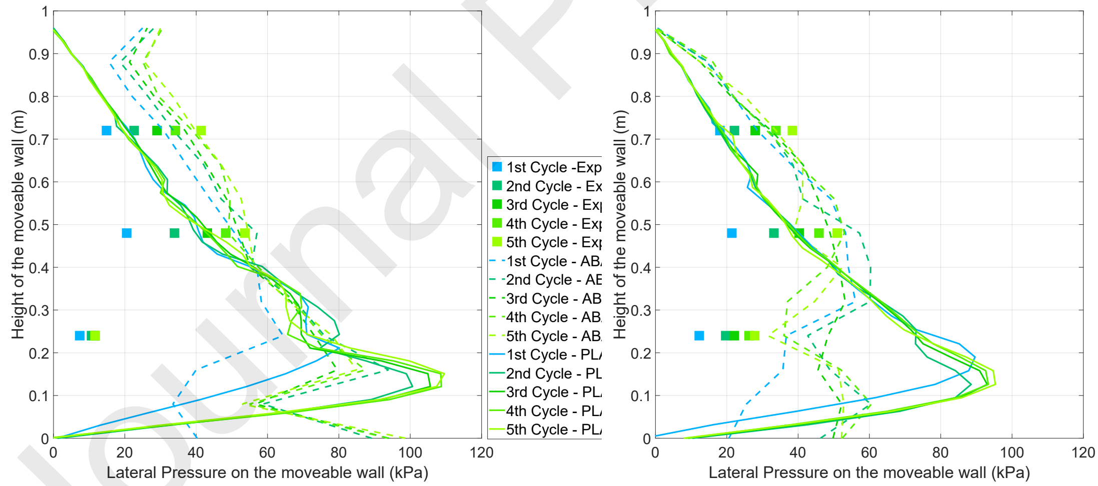

(a) (b)

Figure 11. Lateral earth pressure at the passive stage behind the moveable wall for the test (a) #S2-C-5; (b) #S3-C-5.

As mentioned earlier, the soil-abutment interface is modelled with a more sophisticated approach in ABAQUS with respect to PLAXIS, enabling a more sophisticated modelling of the layered walls leading to a slightly more accurate numerical representation of the sandwich wall in Figure 11b.

The lateral earth pressure curve in PLAXIS is closer to the Rankine assumption, especially at lower depths within the backfill. The maximum lateral earth pressure along the moveable wall within the two models is always on the conservative side with respect to the maximum absolute value observed in the experiment (i.e., leading to higher pressure estimation with respect to the experiment). This shows suitability for preliminary design assessment using simplified approaches with both software packages but also highlights the limitation of a simplified numerical model to accurately mimic the progress of cyclic loads over the life cycle of the structure (e.g., for assessment purposes).

4.4 Failure wedge and boundary condition of test-rig

Comparing the passive position lateral earth pressures in the backfill along the end wall of the rig from experimental and numerical models for #S2-I-12, the maximum value obtained from the numerical models is far larger than that of the experimental tests (almost 300% in ABAQUS and 150% in PLAXIS), especially in case of stiffer walls, see Figure 10b. Furthermore, the comparison with analytical and empirical formulations led to significant differences with higher values of the experimental earth pressure with respect to the empirical and analytical estimations, see Figure 8.

As discussed in section 3.4, the 1-metre length of the rig is not sufficient to allow the development of the full passive failure wedge during the cyclic loading. To investigate the effect of the position of the end wall on the development of passive pressures, further PLAXIS and ABAQUS numerical models were employed to simulate an extension of the box, placing the end wall 2 m from the moveable abutment. The comparison of the lateral earth pressures from experimental tests and simulations with 1-metre and 2-metre boundary conditions is shown in Figure 12 for the #S2-I-12 test.

As expected, the difference between the two boundary conditions becomes significant with increasing cycles; the results also indicate that the boundary condition in the experimental tests increases the earth pressures on the abutment, influencing the comparison with the analytical formulations discussed in section 3.

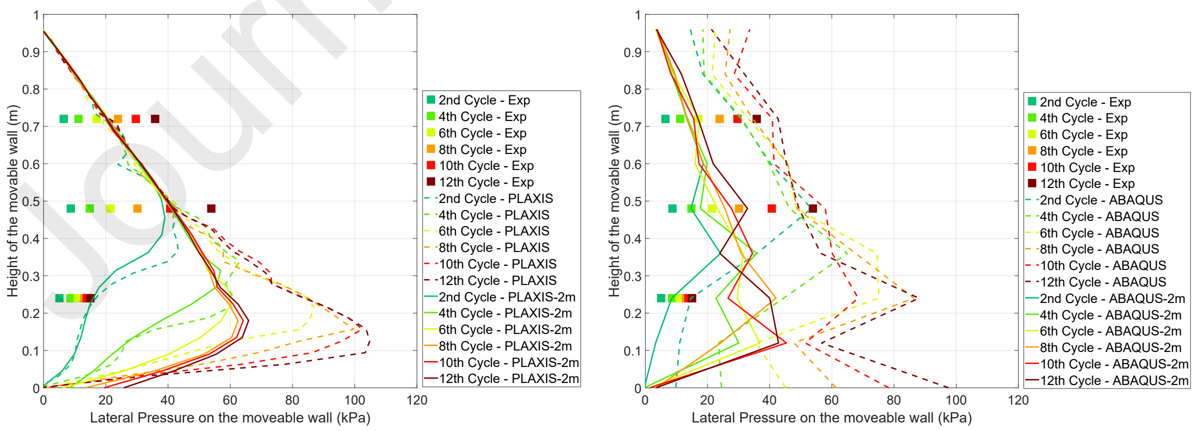

(a) (b)

Figure 12. Lateral earth pressure at the passive stage behind the moveable wall for test #S2-I-12 for the comparison of different backfill sizes in (a) PLAXIS and (b) ABAQUS.

5. Conclusions

This paper considers the effect of different integral bridge abutment wall stiffnesses on the backfill materials and abutment-backfill pressures through a small-scale 1g experimental campaign. The flexibility of the abutment was found to have some influence on the earth pressures measured, increasing its maximum value by more than 25% between a more flexible abutment and a rigid one. The development of earth pressure on the flexible abutment configuration was better captured by a simplified Mohr-Coulomb model in PLAXIS and ABAQUS than for stiffer rigid walls.

The position of the end wall of the 1g rig was found to influence the pressures developed on the movable wall because the rig was not long enough to allow the development of the full passive wedge. The implications of this experimental condition were assessed using the numerical models in PLAXIS and ABAQUS by moving the end wall 1 m further away from the moveable abutment. This was found to reduce the absolute maximum value of the earth pressure on the abutment wall by almost 50%. This result also has implications on the overall experimental-to-analytical comparison carried out between the results of the experimental tests presented in this study and literature and code-based analytical and empirical formulations. Notwithstanding the influence of the boundary condition in the experimental test, the empirical formulation by Dicleli and Albhaisi (2004b) consistently provided a conservative estimate of the experimental data. This suggests a significant degree of conservativeness in this analytical formulation. The relatively simple Mohr-Coulomb constitutive model implemented showed suitability for design purposes with a degree of conservativeness that could be reduced using a more sophisticated soil model. Another factor affecting the accuracy of the numerical results was the estimation of the wall roughness and the wall-to-sand friction in the different soil configurations for which a literature-based estimate was made, and it affected the results significantly. The model was not able to capture the cyclic effect in cases of constant displacements, which is the typical trend of seasonal displacement.

The experimental, analytical, and numerical results shown in this study still emphasise a significant degree of uncertainty and the consequent conservativeness embedded in the currently adopted design and assessment tools. Furthermore, simplified models currently adopted do not allow for capturing changes over the life cycle of the infrastructure (e.g., densification, change in stiffness due to cracking of concrete or atypical boundary conditions due to the presence of other earthworks which could prevent development of failure wedges).

Scaling issues and boundary effects are present in this small-scale experimental campaign limiting more careful consideration of solutions for the design and assessment of earth pressures. Still, results shown allowed the preliminary testing of the experimental approach including measurement methods and the preliminary testing of numerical design tools already available. Larger-scale physical models of integral abutments are required to identify more accurate and less conservative design and assessment of integral bridges. The final aim that can be achieved is to make sure that their advantages as bridge design option can be fully exploited for a robust and less costly transport infrastructure.

Acknowledgements

UK Collaboratorium for Research on Infrastructure and Cities (UKCRIC)–Priming Laboratory EXperiments on Infrastructure and Urban Systems (PLEXUS) was funded by the Engineering and Physical Sciences Research Council under grant number EP/R013535/1, while the Coordination Node for UKCRIC was funded under grant number EP/R017727/1. This funding is gratefully acknowledged, as is the broader thinking on infrastructure systems provided by our UKCRIC colleagues.

Reference

Abate, G, Massimino, M.R., Maugeri, M. and Muir Wood, D. (2010). Numerical Modelling of a Shaking Table Test for Soil-Foundation-Superstructure Interaction by Means of a Soil Constitutive Model Implemented in a FEM Code. Geotech Geol Eng 28:37–59 DOI 10.1007/s10706-009-9275-y

Abdullah, A., & El Naggar, H. (2023). Soil-structure interaction of integral abutments. Transportation Geotechnics, 38, 100900.

Al-Ani M., Murashev A., Palermo A. et al. (2018). Criteria and guidance for the design of integral bridges. Proceedings of the Institution of Civil Engineers – Bridge Engineering 171(3): 143–154, https://doi.org/10.1680/jbren.17.00014

Alampalli, S. and Yannotti, A.P. (1998). In-Service Performance of Integral Bridges and Jointless Decks. *Transportation Research Record: Journal of the Transportation Research Board,* Vol.1624.

Alqarawi, A., Leo, C., Liyanapathirana, D. and Ekanayake, S. (2018). A study on the effects of abutment cyclic movements on the approach of integral abutment bridges. Australian Geomechanics 51(2):1-3.

Anoyatis, G., Di Laora, R., Mandolini, A., & Mylonakis, G. (2013). Kinematic response of single piles for different boundary conditions: analytical solutions and normalisation schemes. Soil Dynamics and Earthquake Engineering, 44, 183-195.

Arsoy, S., Duncan, J.M., & Barker, R.M. (2004). Behavior of a semi integral bridge abutment under static and temperature-induced cyclic loading. Journal of Bridge Engineering, 9(2), 193-199.

Atkinson, J. (2007). *The Mechanics of Soil and Foundations,* London, Taylor & Francis.

Bal, A., Satoglu, S.I. (2018). A goal programming model for sustainable reverse logistics operations planning and an application, Journal of Cleaner Production, Volume 201, 1081-1091, ISSN 0959-6526, https://doi.org/10.1016/j.jclepro.2018.08.104.

Barker K.J. and Carder D.R. (2000). Performance of the Two Integral Bridges Forming the A62 Manchester Road Overbridge. Transport Research Laboratory, Crowthorne, UK, TRL Report 436.

Barker K.J. and Carder D.R. (2001). Performance of an Integral Bridge over the M1–A1 Link Road at Bramham Crossroads. Transport Research Laboratory, Crowthorne, UK, TRL Report 521.

Barker, R.M., Duncan, J.M., Rojiani, K.B., Ooi, P.S., Tan, C.K. and Kim, S.G. (1991). Manuals for the design of bridge foundations: shallow foundations; driven piles; retaining walls and abutments; drilled shafts; estimating tolerable movements; load factor design specifications; and commentary.

Been, K. and Jefferies, M. (2004). Stress dilatancy in very loose sand. *Canadian Geotechnical Journal*, *41*(5), 972-989.

Bhattacharya, S., Demirci, H.E., Nikitas, G., Prakhya, G.K.V., Lombardi, D., Alexander, N. A., ... and Mylonakis, G. (2021). Physical modeling of interaction problems in geotechnical engineering. In Modeling in Geotechnical Engineering, 205-256). Academic Press.

Bolton, M. D., & Powrie, W. (1987). The collapse of diaphragm walls retaining clay. Geotechnique, 37(3), 335-353.

Breña S.F., Bonczar C.H., Civjan S.A., DeJong J.T. and Crovo D.S. (2007) Evaluation of seasonal and yearly behavior of an integral abutment bridge. Journal of Bridge Engineering 12(3): 296–305, https://doi.org/10.1061/(ASCE)1084-0702(2007)12:3(296).

British Standards Institution, BS EN 1991-1-5: 2003: Eurocode 1: Actions on structures: General actions - Thermal actions. London, 2003.

BSI (2004) BS EN 1997-1: Eurocode 7: Geotechnical design. General rules. BSI, London, UK.

BSI (2007) BS EN 1997-2: Eurocode 7: Geotechnical design. Ground investigation and testing. BSI, London, UK.

BSI (2011) PD 6694-1:2011: Recommendations for the design of structures subject to traffic loading to BS EN 1997-1. BSI, London, UK.

Carder, D.R. and Hayes, J.P. (2000). Performance under Cyclic Loading of the Foundations of Integral Bridges. *TRL Report; 433.* Crowthorne: Transport Research Laboratory.

Carville (2023). Available at: https://www.carvilleplastics.com/latest_news/key-properties-acrylic/ (Accessed: 31 Jan 2023).

Cavallaro, A., Fioravante, V., Lanzo, G., Lo Presti D.C.F., Rampello, S., d'Onofrio, A., Santucci De Magistris, F. and Silvestri, F. (2001). Report on the current situation of laboratory stress-strain testing of geomaterials in Italy and its use in practice. Advanced Laboratory Stress-Strain Testing of Geomaterials. Tatsuoka, Shibuya and Kuwano (eds). Balkema, 15-44.

Civjan, S.A., Bonczar, C., Brena, S.F., Dejong, J. and Crovo, D. (2007). Integral Abutment Bridge Behavior: Parametric Analysis of a Massachusetts Bridge. *Journal of Bridge Engineering,* 12**,** 64-71.

Cosgrove E.F. and Lehane B.H. (2003) Cyclic loading of loose backfill placed adjacent to integral bridge abutments. International Journal of Physical Modelling in Geotechnics 3(3): 9–16, https://doi.org/10.1680/ijpmg.2003.030302.

Coulomb CA. Essai sur une application des regles de maximis et minimis a quelqes problemes de stratique relatifs a l' architecture. Memoires de mathematique et de physique. Presentes a l' academie royale des sciences 1776; Paris, 7: p. 343–82.

De Risi, R. (2022). A computational framework for finite element modeling of travelling loads on bridges in dynamic regime. Computer-Aided Civil and Infrastructure Engineering, 37(4), 470-484.

Denton, S., Christie, T., Shave, J. and Kidd, A., (2011). PD 6694-1: Recommendations for the design of structures subject to traffic loading to EN 1997-1. In Bridge Design to Eurocodes: UK Implementation, ICE Publishing, 434-450.

Dhar, S. and Dasgupta, K. (2019). Seismic Soil-Structure Interaction for Integral Abutment Bridges: A Review. Transp. Infrastruct. Geotech. 6, 249–267 . https://doi.org/10.1007/s40515-019-00081-y

Dicleli, M., and Albhaisi, S. M. (2004a). “Effect of cyclic thermal loading on the performance of steel H-piles in integral bridges with stub-abutments.” J. Constr. Steel Res. 60 (2): 161–182. https://doi.org /10.1016/j.jcsr.2003.09.003

Dicleli, M. and Albhaisi, S.M. (2004b). Performance of Abutment-Backfill System under Thermal Variation in Integral Bridges Built on Clay. *Engineering Structures,* 26**,** 949-962.

Dicleli M. and Albhaisi, S.M. (2005). Analytical formulation of maximum length limits of integral bridges on cohesive soils. Canadian Journal of Civil Engineering, 32, 726-38.

Dicleli, M. (2005). Integral Abutment-Backfill Behaviour on Sand Soil-Pushover Analysis Approach. Journal of Bridge Engineering, 10, 354-364.

Duda, A., & Siwowski, T. (2020). Pressure evaluation of bridge abutment backfill made of waste tyre bales and shreds: experimental and numerical study. Transportation Geotechnics, 24, 100366.

England G.L., Tsang N.C.M. and Bush D.I. (2000). Integral Bridges: A Fundamental Approach to the Time–Temperature Loading Problem. Thomas Telford, London, UK.

Ensinger (2023). Available at: https://www.ensingerplastics.com/en-gb/shapes/products/polyethylene-tecafine-pe-500-natural#/product-technical-detail-collapse-item-0-lvl- (Accessed: 31 Jan 2023).

Fiorentino, G., Cengiz, C., De Luca, F., Mylonakis, G., Karamitros, D., Dietz, M., and Nuti, C. (2021). Integral abutment bridges: Investigation of seismic soil-structure interaction effects by shaking table testing. Earthquake Engineering & Structural Dynamics, 50(6), 1517-1538.

Gorini D.N. and Callisto L. (2017). Study of the dynamic soil–abutment–superstructure interaction for a bridge abutment. Proceedings of the 1st European Conference on OpenSees, Porto, Portugal, 57–60.

Gorini D.N. and Callisto L. (2019). A coupled study of soil–abutment–superstructure interaction. In Geotechnical Research for Land Protection and Development: Proceedings of CNRIG 2019 (Calvetti F, Cotecchia F, Galli A and Jommi C (eds)). Springer, Cham, Switzerland, 565–574.

Hassiotis S., Lopez J. and Bermudez R. (2005). Full-scale testing of an integral abutment bridge. In Proceedings of the Federal Highway Association Conference on Integral Abutment and Jointless Bridges, Morgantown, WV, USA, 199–210.

Highways Agency HA (2003). BA 42/96: The design of integral bridges. Highways Agency, Department for Transport, London, UK.

Hoppe E.J. (1999). Guidelines for the Use, Design, and Construction of Bridge Approach Slabs. Virginia Transportation Research Council, Charlottesville, VA, USA, VTRC 00-R4.

Huang, F., Li, L., Javanmardi, A., Zhang, H., & Izadifar, M. (2022). Modified calculation method of earth pressure and internal force of the abutment-pile in integral abutment jointless bridges. Archives of Civil and Mechanical Engineering, 22(4), 205.

Huffman J.T., Xiao F., Chen G. and Hulsey J.L. (2015). Detection of soil–abutment interaction by monitoring bridge response using vehicle excitation. Journal of Civil Structural Health Monitoring 5(4): 389–395.

Javanmardi A, Huang FY, Chen W, Xu P, Xue JQ (2022) Experimental study on seismic response of an integral abutment: Steel H-pile structure under quasi-static cyclic loads. Journal of Earthquake Engineering, DOI: 10.1080/13632469.2022.2112999

Khodair, Y.A., and Hassiotis, S. (2005). Analysis of soil-pile interaction in integral abutment. Computers and Geotechnics, 32(3), 201-209.

Kloukinas, P., Scotto di Santolo, A., Penna, A., Dietz, M., Evangelista, A., Simonelli, A.L., Taylor, C.A. and Mylonakis, G. (2015), Investigation of seismic response of cantilever retaining walls: Limit analysis vs shaking table testing, Soil Dynamics and Earthquake Engineering, 77, 432-445, ISSN 0267-7261, https://doi.org/10.1016/j.soildyn.2015.05.018.

Kramer, S.L. (1996). Geotechnical earthquake engineering. Pearson Education India.

LaFave, J.M., Brambila, G., Kode, U., Liu, G., and Fahnestock, L.A. (2021). Field behavior of integral abutment bridges under thermal loading. Journal of Bridge Engineering, 26(4), 04021013.

Lawver, A., French, C. and Shield, C.K. (2000). Field Performance of Integral Bridge. *Transportation Research Record: Journal of the Transportation Research Board,* 1740**,** 108-117.

Lehane B.M. (2011). Lateral soil stiffness adjacent to deep integral bridge abutments. Géotechnique 61(7), 593–603, https://doi.org/10.1680/geot.9.P.135

Lehane, B.M., Keogh, D.L., and O'Brien, E.J. (1999). Simplified elastic model for restraining effects of backfill soil on integral bridges. Computers & structures, 73(1-5), 303-313.

Lings, M.L. and Dietz, M.S. (2004). An improved direct shear apparatus for sand. Géotechnique, 54(4), 245-256.

Liu, H., Han, J., & Parsons, R. L. (2022). Settlement and horizontal earth pressure behind model integral bridge abutment induced by simulated seasonal temperature change. Journal of Geotechnical and Geoenvironmental Engineering, 148(6), 04022043.

Lock R.J. (2002). Integral Bridge Abutments. Department of Engineering, University of Cambridge, Cambridge, UK.

Luo S., De Luca F., De Risi R., Le Pen L., Watson G., Milne D., Chapman D., Sextos A., Cassidy N., Jefferson I., Metje N., Smethurst J., Richards D., Mylonakis G., Taylor C., Powrie W., and Rogers C.D.F. (2022). Challenges and perspectives for integral bridges in the UK: PLEXUS small-scale experiments. Proceedings of the Institution of Civil Engineers Smart Infrastructure and Construction, https://doi.org/10.1680/jsmic.21.00020

Manzari, M.T. and Dafalias, Y.F., (1997). A critical state two-surface plasticity model for sands. *Géotechnique*, *47*(2), 255-272.

Massachusetts Department of Transportation (1999). Massachusetts Bridge Manual, Part I. Mass DOT, Boston, MA, USA.

Mylonakis, G., Kloukinas, P., & Papantonopoulos, C. (2007). An alternative to the Mononobe–Okabe equations for seismic earth pressures. Soil Dynamics and Earthquake Engineering, 27(10), 957-969.

Muttoni A., Dumont A.G., Burdet O., Savvilotidou M., Einpaul J. and Nguyen M.L., (2013). Experimental Verification of Integral Bridge Abutments. Office Fédéral des Routes, Ittigen, Switzerland.

Navfac (1982) Foundations and Earth Structures Design Manual 7.2., Naval Facilities Engineering Systems Command, Department of the Navy, Alexandria, VA, USA.

Neville, A.M. (1995). *Properties of concrete,* Harlow, Longman Scientific & Technical.

Ng C.W.W., Springman S.M. and Norrish A.R.M. (1998). Centrifuge modelling of spread-base integral bridge abutments. Journal of Geotechnical and Geoenvironmental Engineering 124, 376–388, https://doi.org/10.1061/(ASCE)1090-0241(1998)124:5(376).

Paraschos, A. (2016). Effects of Wingwall Configurations of the Behaviour of Integral Abutment Bridges. PhD thesis, University of Maryland, College Park, MD, USA.

Paul, M., Laman, J.A. and Linzell, D.G. (2005) Thermally induced superstructure stresses in prestressed girder integral abutment bridges. Transportation Research Board - 6th International Bridge Engineering Conference: Reliability, Security, and Sustainability in Bridge Engineering, July 17, 2005 - July 20, Boston, MA, United states. Transportation Research Board, 287-297.

Petursson, K. and Kerokoski, P. (2011) Monitoring and analysis of abutment-soil interaction of two integral bridges. J. Bridg. Eng. 18(1), 54–64.

PLAXIS manuals (2019). Tutorial Manual Connect Edition V20.Potyondy J.G. (1961). Skin friction between various soils and construction materials. Géotechnique, 11(4), 339-353.

Powrie, W. (2004). Soil Mechanics: Concepts and Applications, Second Edition (2nd ed.). CRC Press. https://doi.org/10.4324/9780203461525

Rees, D.W. (2009). Mechanics of optimal structural design: minimum weight structures. John Wiley & Sons.

Rowe, P.W. (1952). Anchored sheet pile walls. Proceedings of the institution of Civil Engineers, Pt 1, 1,27-70.

Ryall, M.J., Parke, G. A. R. and Harding, J.E. (eds.) (2000). The Manual of Bridge Engineering, London: Thomas Telford.

Sadrekarimi, A. and Olson, S.M. (2011) Yield strength ratios, critical strength ratios, and brittleness of sandy soils from laboratory tests, Canadian Geotechnical Journal 48(3), 493-510, https://cdnsciencepub.com/doi/abs/10.1139/T10-078

Sakhare, A., Punetha, P., Meena, N. K., Nimbalkar, S., & Dodagoudar, G. R. (2023). Dynamic Behaviour of Integral Abutment Bridge Transition under Moving Train Loads. Transportation Geotechnics, 100989.

Sandberg J., Magnino L., Nowak P., Wiechecki M. and Thusyanthan I. (2020). The integral bridge design concept for the third runway at Heathrow, UK. Proceedings of the Institution of Civil Engineers–Bridge Engineering, 173(2), 112–120, https://doi.org/10.1680/jbren.19.00044

Sigdel, L.D., Al-Qarawi, A., Leo, C.J., Liyanapathirana, S. and Hu, P. (2021). Geotechnical Design Practices and Soil–Structure Interaction Effects of an Integral Bridge System: A Review. Appl. Sci. , 11, 7131. https:// doi.org/10.3390/app11157131

Silva, P. H., Costa, Y. D., Walter, J. R., Kouchaki, B. M., Zornberg, J. G., & Costa, C. M. (2023). Numerical Evaluation of a Semi-Integral Bridge Abutment Under Cyclic Thermal Movements. Transportation Geotechnics, 100938.

Skorpen S.A., Kearsley E.P. and Kruger E.J. (2018). Measured temperature and shrinkage effects on a 90 m long integral bridge in South Africa. Proceedings of the Institution of Civil Engineers – Bridge Engineering 171(3): 169–178, https://doi.org/10.1680/jbren.17.00019.

Sonelastic (2023). Available at: https://www.sonelastic.com/en/fundamentals/tables-of-materials-properties/woods.html (Accessed: 31 Jan 2023).

Springman S.M., Norrish A.R.M. and Ng C.W.W. (1996). Cyclic Loading of Sand behind Integral Bridge Abutments. Transport Research Laboratory, Crowthorne, UK, TRL Report 146.

Stanier, S.A., Blaber, J., Take, W.A, and White, D.J. (2015) Improved image-based deformation measurement for geotechnical applications. Canadian Geotechnical Journal. 53(5): 727-739. https://doi.org/10.1139/cgj-2015-0253

Walter, J.R., Morsy, A.M. and Zornberg, J.G. (2018). Experimental and Numerical Investigation of Lateral Earth Pressures Generated from Repeated Loading. IFCEE 2018: Recent Developments in Geotechnical Engineering Practice, 158-168. https://ascelibrary.org/doi/abs/10.1061/9780784481608.016

White, H., Ptursson, H. and Collin, P. (2010). Integral abutment bridges: The European way. *Practice Periodical on Structural Design and Construction,* 15**,** 201-208.

Wood, D.M. (2004). *Geotechnical Modeling,* London, E & FN Spoon.

Wood, D.M. and Nash, D. (2000). Earth Pressure on an Integral Bridge Abutment; A Numerical Case Study. *Soils and Foundation; The Japanese Geotechnical Society,* 40**,** 23-38.

Xue J. Q., Lin Y. B., Briseghella B. and Huang F. Y. (2022). Quasi-static Test on Mechanical Behaviors of Pre-hole Isolation Pile-soil Interaction. China Journal of Highway and Transport, 35(4): 153-165.

Physical and numerical investigation of integral bridge abutment stiffness due to seasonal thermal loading

Sha Luo[1], Ziyan Huang[2], Yazan Asia[2,4], Flavia De Luca[2], Raffaele De Risi[2], John Harkness[3], Louis Le Pen[3], Geoff Watson[3], David Milne[3], David Chapman[1], Anastasios Sextos[2], Nicole Metje[1], George Mylonakis[2,5], Nigel Cassidy[1], Ian Jefferson[1], Joel Smethurst[3], David Richards[3], Colin Taylor[2], William Powrie[3], Christopher Rogers[1]

[1] School of Engineering, University of Birmingham, Edgbaston, B15 2TT (UK)

[2]School of Civil, Aerospace and Mechanical Engineering, University of Bristol, Queens Building, BS8 1TR (UK)

[3] School of Engineering, University of Southampton, Southampton, UK

[4]Department of Engineering, University of Cambridge, UK

[5] Department of Civil Infrastructure and Environmental Engineering Khalifa University, Abu Dhabi, UAE

CRediT author statement

Sha Luo: Conceptualization, Methodology, Investigation, Validation, Formal Analysis, Data Curation, Software, Visualisation, Writing Original Draft, Writing - Review & Editing.

Ziyan Huang: Conceptualization, Methodology, Data Curation, Software, Visualisation, Writing Original Draft, Writing - Review & Editing.

Yazan Asia: Conceptualization, Methodology, Data Curation, Investigation, Writing - Review & Editing.

Flavia De Luca: Conceptualization, Methodology, Investigation, Formal Analysis, Visualisation, Supervision, Project Administration, Writing - Review & Editing.

Raffaele De Risi: Conceptualization, Methodology, Investigation, Formal Analysis, Data Curation, Software, Visualisation, Supervision, Writing - Review & Editing.

John Harkness: Conceptualization, Methodology, Validation, Writing - Review & Editing.

Louis Le Pen: Conceptualization, Methodology, Investigation, Writing - Review & Editing.

Geoff Watson: Conceptualization, Methodology, Investigation, Writing - Review & Editing.

David Milne: Conceptualization, Methodology, Validation, Writing - Review & Editing.

David Chapman: Conceptualization, Methodology, Supervision, Project Administration, Writing - Review & Editing.

Anastasios Sextos: Conceptualization, Methodology, Validation, Supervision, Project Administration, Writing - Review & Editing.

Nicole Metje: Conceptualization, Methodology, Supervision, Project Administration, Writing - Review & Editing.

George Mylonakis: Conceptualization, Methodology, Validation, Formal Analysis, Supervision, Project Administration, Writing - Review & Editing.

Nigel Cassidy: Conceptualization, Methodology, Investigation, Project Administration, Writing - Review & Editing.

Ian Jefferson: Conceptualization, Methodology, Project Administration, Writing - Review & Editing.

Joel Smethurst: Conceptualization, Methodology, Project Administration, Writing - Review & Editing.

David Richards: Conceptualization, Methodology, Project Administration, Writing - Review & Editing.

Colin Taylor: Conceptualization, Methodology, Supervision, Project Administration, Writing - Review & Editing.

William Powrie: Conceptualization, Methodology, Validation, Supervision, Project Administration, Writing - Review & Editing.

Christopher Rogers: Conceptualization, Methodology, Supervision, Project Administration, Writing - Review & Editing, Funding acquisition.

Term	***Definition***
Conceptualization	*Ideas; formulation or evolution of overarching research goals and aims*
Methodology	*Development or design of methodology; creation of models*
Software	*Programming, software development; designing computer programs; implementation of the computer code and supporting algorithms; testing of existing code components*
Validation	*Verification, whether as a part of the activity or separate, of the overall replication/ reproducibility of results/experiments and other research outputs*
Formal analysis	*Application of statistical, mathematical, computational, or other formal techniques to analyze or synthesize study data*
Investigation	*Conducting a research and investigation process, specifically performing the experiments, or data/evidence collection*
Resources	*Provision of study materials, reagents, materials, patients, laboratory samples, animals, instrumentation, computing resources, or other analysis tools*
Data Curation	*Management activities to annotate (produce metadata), scrub data and maintain research data (including software code, where it is necessary for interpreting the data itself) for initial use and later reuse*
Writing - Original Draft	*Preparation, creation and/or presentation of the published work, specifically writing the initial draft (including substantive translation)*

Term	Definition
Writing - Review & Editing	*Preparation, creation and/or presentation of the published work by those from the original research group, specifically critical review, commentary or revision – including pre-or postpublication stages*
Visualization	*Preparation, creation and/or presentation of the published work, specifically visualization/ data presentation*
Supervision	*Oversight and leadership responsibility for the research activity planning and execution, including mentorship external to the core team*
Project administration	*Management and coordination responsibility for the research activity planning and execution*
Funding acquisition	*Acquisition of the financial support for the project leading to this publication*

Declaration of interests

☒ The authors declare that they have no known competing financial interests or personal relationships that could have appeared to influence the work reported in this paper.

☐The authors declare the following financial interests/personal relationships which may be considered as potential competing interests: